

SPINS: A Structural Priors aided Inertial Navigation System

Yang Lyu, Thien-Minh Nguyen, Liu Liu, Muqing Cao,
Shenghai Yuan, Thien Hoang Nguyen and Lihua Xie, *Fellow, IEEE*

Abstract—Although Simultaneous Localization and Mapping (SLAM) has been an active research topic for decades, current state-of-the-art methods still suffer from instability or inaccuracy due to feature insufficiency or its inherent estimation drift, in many civilian environments. To resolve these issues, we propose a navigation system combining the SLAM and prior-map-based localization. Specifically, we consider additional integration of line and plane features, which are ubiquitous and more structurally salient in civilian environments, into the SLAM to ensure feature sufficiency and localization robustness. More importantly, we incorporate general prior map information into the SLAM to restrain its drift and improve the accuracy. To avoid rigorous association between prior information and local observations, we parameterize the prior knowledge as low dimensional *structural priors* defined as relative distances/angles between different geometric primitives. The localization is formulated as a graph-based optimization problem that contains sliding-window-based variables and factors, including IMU, heterogeneous features, and structure priors. We also derive the analytical expressions of Jacobians of different factors to avoid the automatic differentiation overhead. To further alleviate the computation burden of incorporating structural prior factors, a selection mechanism is adopted based on the so-called *information gain* to incorporate only the most effective structure priors in the graph optimization. Finally, the proposed framework is extensively tested on synthetic data, public datasets, and, more importantly, on the real UAV flight data obtained from a building inspection task. The results show that the proposed scheme can effectively improve the accuracy and robustness of localization for autonomous robots in civilian applications.

Index Terms—Localization, SLAM, structure prior, navigation, optimization.

I. INTRODUCTION

Autonomous vehicles, especially Unmanned Aerial Vehicles (UAVs), have attracted tremendous research interests in recent years due to their potential in improving efficiency and safety in many military and civilian applications [1]. One fundamental prerequisite for an autonomous vehicle to successfully execute missions is to accurately and reliably estimate its 6-DOF pose [2]. Due to physical and electromagnetic interferences, GPS systems may not provide persistent and reliable localization information in many complex environments, named as

GPS-denied environments, making it a challenging task for a vehicle to carry out missions autonomously.

There are mainly two approaches to handle the localization in a GPS-denied environment. The first approach is the simultaneous localization and mapping (SLAM) framework [3], which is to incrementally track the local pose by estimating the relative transformation between two frames. The main drawback of SLAM based method is that the localization result drifts as time goes on due to the accumulated relative pose estimation errors [4]. Another alternative is to localize the vehicle according to a prior map by matching the local observations to the map directly [5]. Although this method has no drift issue, it needs a prior map with an acceptable level of accuracy and proper associations between local observations and the prior map; therefore, it may be vulnerable to challenging observation conditions [6]. Reflecting on the pros and cons of the two distinct approaches, it is a good practice to combine them, namely, to lend some prior information of the map to aid the SLAM based navigation. A loosely coupled framework is proposed in [7], which incorporates global pose factors in the local SLAM optimization. The global pose is obtained by matching images with a global map. As per the authors' knowledge, only [8] uses a locally pre-stored 3D points cloud map to fix the drift of a local SLAM in a tightly coupled framework.

Nevertheless, both the SLAM and prior map based localization that is based only on point features may fail, primarily, due to the feature insufficiency in a low texture environment. Line and plane features are considered as promising supplements to point features for robot localization, especially in civilian environments. First, lines and planes are more structurally salient and therefore can be endowed with more prior information. Secondly, they are more stable than points with respect to lighting/texture changes. Finally, lines and planes are more ubiquitous in the structural environment, such as most infrastructures in urban cities. Thus, it is a good practice to additionally integrating line and plane in the localization framework.

This paper proposes a Structure Priors aided Inertial Navigation System (SPINS) based on point, line, and plane features, to deal with the localization problem of autonomous vehicles operated in civilian environments. The SPINS is a tightly-coupled framework that combines SLAM and prior map based localization by lending feature level structure prior information to restrain the drift of the SLAM based methods. It's non-trivial to achieve the combination in practical autonomous robot application. First, the prior-map-based localization re-

The work is supported by National Research Foundation (NRF) Singapore, ST Engineering-NTU Corporate Lab under its NRF Corporate Lab@ University Scheme.

Yang Lyu, Thien-Minh Nguyen, Muqing Cao, Shenghai Yuan, Thien Hoang Nguyen and Lihua Xie (corresponding author) are with School of Electrical and Electronic Engineering, Nanyang Technological University, 50 Nanyang Avenue, Singapore 639798. (Email: lyu.yang@ntu.edu.sg)

Liu Liu is with College of Engineering and Computer Science, Australian National University, Canberra ACT 0200, Australia.

quires a high fidelity map that may not be available in many scenarios. Even if it is available, the association between local observations of heterogeneous features and the geometric primitives extracted from the map is also challenging [9]. In addition to the above challenges, the prior information may be in large amounts and very redundant. It is important to determine what kind of prior information to integrate into the local SLAM, which already poses a heavy burden to the onboard computation resources of the autonomous vehicle.

To solve the first problem, we broaden the sources of prior information from maps to more generalized prior knowledge, ranging from the elaborated CAD blueprints to some coarse, shared knowledge, such as parallel or orthogonal lines/planes. To build associations between the prior information and the observed point, line, and plane features, rather than carrying out feature matching based on high dimensional descriptors [10] to directly introduce global poses, we parameterize the prior information as pairwise distances and angles between different geometric primitives, so that the association and integration to SLAM can be straightforward. To reduce the computation burden of incorporating too many structure priors, we propose to implement an information-theoretic metric to measuring the contribution of each structure prior to the localization, and hereafter, to integrate the most useful n structure priors. To summarize, this paper makes the following contributions:

- 1) Firstly, we proposed a tightly coupled localization framework that combines the SLAM and prior-map-based localization. We integrate point, line, and plane features into the SLAM to improve its accuracy and robustness. More importantly, we incorporate more generalized prior map information into the local SLAM through the feature level *structure priors*, which are defined as the relative distances/angles between different geometric primitives.
- 2) Secondly, the localization problem is solved in a sliding window fashion with the state-of-the-art factor graph optimization solver [11]. To enable the integration of heterogeneous features and the structural priors, we derive the analytical expressions of the measurement Jacobians to avoid imposing runtime overhead of the automatic differentiation methods [12].
- 3) Moreover, to ease the burden of solving a graph-based optimization problem with various factors, we develop a structure prior information selection strategy based on the *information gain* to incorporate only the most effective structure priors for localization.
- 4) Finally, we test our proposed framework extensively based on synthetic data, public datasets, and real UAV flight data obtained from a building inspection task. The results indicate that the proposed framework can improve the localization robustness and even in challenging environments.

The remainder of the paper is organized as follows. In Section II, the related works are provided. The proposed SPINS framework is formulated in Section III. The geometric features and structure priors are modeled in Section IV and Section V, respectively. The structure priors selection strategy is designed in Section VI. Experiment validations are provided

in Section VII. Section VIII concludes the paper.

II. RELATED WORKS

SLAM based localization is considered as one of the most promising approaches for robot localization. By measuring salient features from the environment, the robot can accumulatively estimate its pose in local coordinates, which is preferred in many challenging environments, such as complex indoor or urban cities [13]. In this part, we review the recent SLAM results based on different features and the integrated structure priors.

Among existing methods reported in the literature, the point feature is the most commonly used in the environment perception front-end in SLAM frameworks, especially in the visual aided navigation frameworks. Some successful demonstrations, such as ORB-SLAM [14], and VINS-mono [15], utilize 2D point features from vision sensors to estimate the local motion and sparse 3D point clouds of the environment. With the development of more advanced 3D sensing technologies, navigation methods based on 3D sensors, such as stereo-vision [16], LiDAR [17], and RGB-D camera [18], can directly utilize 3D points with metric information in the estimation process, therefore can provide improved localization and reconstruction results. In addition to the most commonly used point features, line and plane features are also adopted as additional features in some particular mission scenarios, such as indoor servicing [19], [20], structure inspection [21], [22], and autonomous landing [23], in case that point features are not sufficient.

In the past few years, SLAM methods using heterogeneous features have begun to draw researchers' attention. The improvement of localization performance has been verified by works with different feature combinations. In vision-based SLAM, line features are considered effective to point features in a low textural but high structural environment with a proper definition of the state and re-projection error. Extending from the ORB-SLAM, the PL-SLAM [24] can simultaneously handle both point and line correspondences. The line state is parameterized with its endpoints, and the re-projection error is defined as point-to-plane distances between the projected endpoints of 3D line and the observed line on image plane. A tightly coupled Visual Inertial Odometry (VIO) exploiting both point and line features is proposed in [25]. The line is parameterized as a six-parameter Plücker coordinate [26] for transformation and projection simplicity, and a four-parameter orthonormal representation for optimization compactness. Similar reprojection error to [24] is utilized in [25]. Comparisons of different line feature parameterization are provided in [27] based on the MSCKF SLAM framework, which shows that the closest point (CP) based [28] and quaternion based [29] representations outperform the Plücker representation under noisy measurement conditions. Besides the monocular based methods above, a stereovision-based VIO using point and line features together is proposed in [30], the measurement model is directly extended from the monocular camera model similar to [24]. In the stereo vision based PL-SLAM framework [31], a visual odometry is formulated similarly to [30]. In addition to that, the key-frame selection

and loop closure detection under point and line features setup are also provided.

As 3D sensors such as LiDAR or RGB-D camera becomes more popular, plane features now can be effectively extracted in a man-made environment. A Lidar Odometry and Mapping (LOAM) in real-time is proposed in [17], which utilizes plane features to improve the registration accuracy of a point cloud. A LiDAR-inertial SLAM framework based on 3D planes is proposed in [32], where the closest point representation is utilized for parameterizing a plane. A tightly-coupled vision-aided inertial navigation framework combining point and plane features is proposed in [33], where the plane is parameterized similar to [32]. In addition to that, the point-on-plane constraint is incorporated to improve the VINS performance. Recently, the point, line, and plane features are jointly applied in the SLAM frameworks [34]–[37] to realize stable localization and mapping in low texture environments. In [34], the line and plane features are tracked simultaneously along a long distance to provide persistent measurements. Also, the relationship between features, such as co-planar points, is implemented to enforce structure awareness. Similar work [36] utilizes line and plane to improve the feature richness and incorporates more spatial constraints to realize more robust visual inertial odometry. A pose-landmark graph optimization back-end is proposed in [37] based on the three types of features, which are handled in a unified manner in [38]. A thorough theoretical analysis of implementing point, line, and plane features in VINS is provided in [27]. The three kinds of features are parameterized as measurements to estimate the local state based on a recursive MSCKF framework. More importantly, the observability analysis of different combinations of features is provided, and the effect of degenerate motion is studied.

Although researchers have begun to introduce heterogeneous geometric features into their SLAM works, integrating prior map information to the localization still draws limited attention. There are mainly two types of prior information that can be obtained from a prior map to aid the SLAM, namely the global information and the local structure information. By incorporating global pose constraints by matching local observations with a consistent global map, the SLAM drift can be reduced. Inspiring by this, the global information is incorporated in the local SLAM in both loosely coupled manner [7] and tightly coupled manner [8]. On the other hand, only limited structural priors information, such as point-on-line, line-on-plane, and point-on-plane constraints, are considered in the SLAM. Note that the structure information is ubiquitous in civil environments that are rich of man-made objects. It is practical wisdom to implement more general structure prior information of the environment to improve the localization and mapping quality rather than to consider the environment as entirely unknown. For instance, in a building inspection environment, the structure information, as elaborate as the CAD modes, or as coarse as some common sense such as flat planes, parallel lines, with proper parameterization, can be implemented to aid the SLAM process [21], [39].

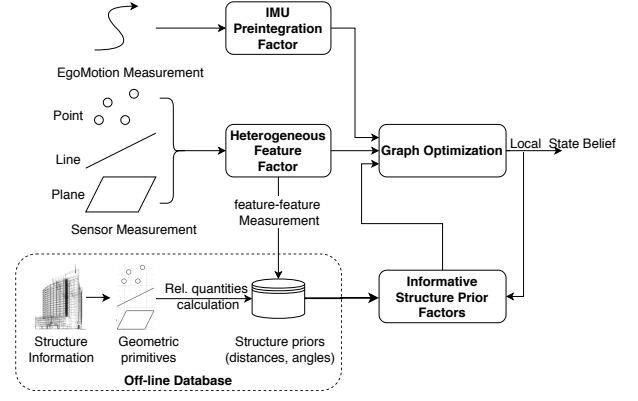
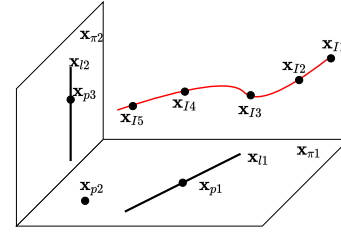
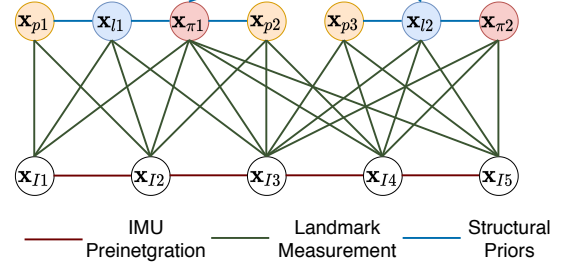


Fig. 1: The systematic functional block of the proposed SPINS framework.



(a) A geometric representation of point, line and plane features.



(b) The corresponding factor graph of subfigure (a).

Fig. 2: The factor graph including the structural priors.

III. SYSTEM DESCRIPTION

In this section, the SPINS is described from a systematic point of view. The functional blocks of the system are illustrated in Fig. 1. The SPINS depends on three types of information to fulfill the task of accurately and reliably localizing an autonomous vehicle in a challenging civilian environment, which are 1) ego-motion measurements from interoceptive sensors, such as the Inertial Measurement Unit (IMU), at high-frequency feeding streaming, and 2) detected/tracked point, line, and plane features from exteroceptive sensors, and 3) structure priors which are parameterized as pairwise high fidelity measurements between features.

A. Optimization formulation

The aforementioned three types of information within a sliding window are incorporated into a factor graph, which is a bipartite graph contains variables and factors. Specifically, the variables represent the state of the local vehicle and the heterogeneous feature, and factors encode different types of

observations and structural priors. The states included in the sliding window at time t are defined as

$$\mathcal{X}_t \triangleq [\{\mathbf{x}_{I,m}^\top\}_{m \in T_t}, \{\mathbf{x}_i^\top\}_{i \in P_t}, \{\mathbf{x}_j^\top\}_{j \in L_t}, \{\mathbf{x}_k^\top\}_{k \in \Pi_t}]^\top, \quad (1)$$

where $\{\mathbf{x}_{I,m}\}_{m \in T_t}$ contains active IMU states within the sliding window at time instance t . T_t denotes the set of IMU measurements at t . P_t, L_t, Π_t denote the sets of point, line and plane features that are observed within the sliding window at time t , respectively. The IMU state is

$$\mathbf{x}_I \triangleq [{}_G^I \bar{q}^\top \quad {}^G \mathbf{p}_I^\top \quad {}^G \mathbf{v}_I^\top \quad \mathbf{b}_g^\top \quad \mathbf{b}_a^\top]^\top, \quad (2)$$

where ${}_G^I \bar{q}$ is a unite quaternion denotes the rotation from the global frame $\{G\}$ to the IMU frame $\{I\}$. ${}^G \mathbf{p}_I$ and ${}^G \mathbf{v}_I$ are the IMU position and velocity, respectively. $\mathbf{b}_g, \mathbf{b}_a$ are the random walk biases for gyroscope and accelerometer, respectively. With the state definition (1), the objective is to minimize the cost function of different measurement residuals in (3).

$$\begin{aligned} \min_{\mathcal{X}_t} & \left\{ \|\mathbf{r}_p\|_{\mathbf{P}_p}^2 + \sum_{m \in T_t} \|\mathbf{r}_{I,m}\|_{\Sigma_m}^2 \right. \\ & + \sum_{i \in P_t} \rho(\|\mathbf{r}_i\|_{\Sigma_i}^2) + \sum_{j \in L_t} \rho(\|\mathbf{r}_j\|_{\Sigma_j}^2) + \sum_{k \in \Pi_t} \rho(\|\mathbf{r}_k\|_{\Sigma_k}^2) \\ & \left. + \sum_{s \in \mathcal{S}_t} \rho(\|\mathbf{r}_s\|_{\Sigma_s}^2) \right\}. \end{aligned} \quad (3)$$

The first term of (3) is the cost on prior estimation residuals, and \mathbf{P}_{p_t} is the corresponding covariance prior to the optimization at t [40]. The second term is the cost of IMU-based residual, and $\mathbf{r}_{I,m}$ defines the measurement residual between active frames m and $m+1$. The IMU measurement between time step m and $m+1$ is obtained by integrating high-frequency raw IMU measurements continuously with the technique called IMU preintegration [41], and Σ_m is the corresponding measurement covariance. The second line of (3) represents the cost function of measurement residuals of point, line, and plane features and are weighted by their corresponding covariances. The third line is the cost of structure priors measurement residuals.

For a measurement in Euclidean space, a residual term is defined as the difference between the predicted measurement based on estimated state $\hat{\mathcal{X}}$ and a real measurement \mathbf{z} , as

$$\mathbf{r} = h(\hat{\mathcal{X}}) - \mathbf{z}, \quad (4)$$

where $h(\cdot)$ is the measurement prediction function for the estimated state between any two variables in the factor graph. The term $\|\mathbf{r}\|_{\Sigma}^2 = \mathbf{r}^\top \Sigma^{-1} \mathbf{r}$ is defined as the squared Mahalanobis distance with covariance matrix Σ . A huber loss $\rho(\cdot)$ [42] is applied on each squared term to reduce potential mismatches between states and measurements. The optimization of (3) is usually solved with an iterative Least-Squares solver through a linear approximation. In the non-Euclidean space \mathcal{X} , the approximation is achieved by expanding the residual around the origin of a chart computed at current estimation $\hat{\mathcal{X}}$ as

$$\begin{aligned} \mathbf{r}(\hat{\mathcal{X}} \boxplus \Delta \mathcal{X}) & \approx \mathbf{r}(\hat{\mathcal{X}}) + \frac{\partial \mathbf{r}(\hat{\mathcal{X}} \boxplus \Delta \mathcal{X})}{\partial \Delta \mathcal{X}}|_{\Delta \mathcal{X}=\mathbf{0}} \Delta \mathcal{X} \\ & = \mathbf{r}(\hat{\mathcal{X}}) + \mathbf{J} \Delta \mathcal{X}. \end{aligned} \quad (5)$$

The operator \boxplus applies a perturbation $\Delta \mathcal{X}$ to the manifold space \mathcal{X} . Specifically, for the Euclidean states, the \boxplus operator degenerates to the vector addition operator. The \mathbf{J} is the sparse Jacobian matrix with only none zero block on the related two states. Incorporating the approximation (5) to (3), we have the following form

$$\Delta \mathcal{X}^\top \mathbf{H} \Delta \mathcal{X} + 2\mathbf{b}^\top \Delta \mathcal{X} + \text{const}(\hat{\mathcal{X}}), \quad (6)$$

where

$$\begin{aligned} \mathbf{H} = & \mathbf{J}_p^\top \mathbf{P}_p^{-1} \mathbf{J}_p + \sum_{m \in T_t} \mathbf{J}_m^\top \Sigma_m^{-1} \mathbf{J}_m \\ & + \sum_{i \in P_t} \mathbf{J}_i^\top \Sigma_i^{-1} \mathbf{J}_i + \sum_{j \in L_t} \mathbf{J}_j^\top \Sigma_j^{-1} \mathbf{J}_j + \sum_{k \in \Pi_t} \mathbf{J}_k^\top \Sigma_k^{-1} \mathbf{J}_k \\ & + \sum_{s \in \mathcal{S}_t} \mathbf{J}_s^\top \Sigma_s^{-1} \mathbf{J}_s, \end{aligned}$$

and

$$\begin{aligned} \mathbf{b} = & \mathbf{r}_p^\top \mathbf{P}_p^{-1} \mathbf{J}_p^\top + \sum_{m \in T_t} \mathbf{r}_m^\top \Sigma_m^{-1} \mathbf{J}_m^\top \\ & + \sum_{i \in P_t} \mathbf{r}_i^\top \Sigma_i^{-1} \mathbf{J}_i^\top + \sum_{j \in L_t} \mathbf{r}_j^\top \Sigma_j^{-1} \mathbf{J}_j^\top + \sum_{k \in \Pi_t} \mathbf{r}_k^\top \Sigma_k^{-1} \mathbf{J}_k^\top \\ & + \sum_{s \in \mathcal{S}_t} \mathbf{r}_s^\top \Sigma_s^{-1} \mathbf{J}_s^\top, \end{aligned}$$

and $\text{const}(\hat{\mathcal{X}})$ is a constant term relies only on $\hat{\mathcal{X}}$.

As a result, (6) can be minimized by solving

$$(\mathbf{H} + \lambda \mathbf{I}) \Delta \mathcal{X} = -\mathbf{b}, \quad (7)$$

where λ is a damping factor. The estimation is hereafter updated as

$$\hat{\mathcal{X}} = \hat{\mathcal{X}} \boxplus \Delta \mathcal{X}. \quad (8)$$

The update iterates until converges. The formulation of measurement functions $h(\cdot)$ with regard to the geometric features and the structural priors are provided in IV and Section V, respectively.

B. Structure prior information

The information that can be considered as structural priors is ubiquitous, ranging from the fine-grained blueprint to common knowledge such as parallel lines or planes. The greatest challenge to integrate the prior information in the optimization is to correctly associate the structure information with the observed features. Benefiting from using point, line, and plane features simultaneously, we can parameterize the spatial relationship between different geometric features as pairwise relative distances and angles in Section V. The advantages of using such parameterization are mainly two folds. Firstly, with simple angles and distances, the rigorous association process between the structure priors and observed features can be avoided. Secondly, with the relative distances and angles, more general structural relationships between different geometric primitives, besides some specific constraint, such as point-on-plane or line-on-plane constraint, can be expressed concisely.

The structural priors can be obtained offline based on the following three steps:

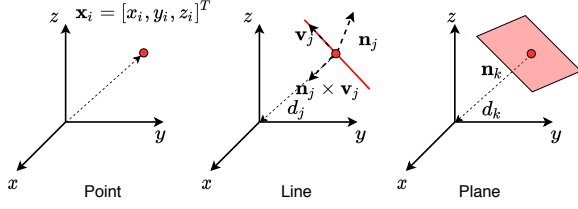


Fig. 3: The geometry representation of point, line and plane in 3D space.

- 1) extract structural primitives from various forms, *e.g.*, high fidelity maps, local measurements, semantic information *etc.*,
- 2) measure and calculate the relative quantities between every two primitives (as formulated in Section V), and
- 3) store the quantities (distances/angles) as structure priors in a database.

In the online localization process, a structural prior is integrated into the optimization when a distance or an angle calculated from two features' estimates is close enough to any candidates in the structure prior database.

Remark 1. In many civilian environment, most of the structure patterns are inerratic and repetitive. As a result, the angles and distances' distributions are sparse and it is easy to associate them with observed feature patterns. An illustrative example is shown in Fig.7 and Fig.8, where Fig.7 shows extracted planes from ground truth point cloud of the EuRoC Datasets [43], and Fig.8 shows the angles and distances between planes derived from randomly sampled points of the point cloud.

IV. HETEROGENEOUS GEOMETRIC FEATURES

In this section, we discuss how to model the point, line, and plane features based on on-board perception and corresponding factorization into the graph optimization.

A. Point Feature

As one of the most frequently implemented features in perception tasks, a point feature can be uniquely parameterized by its 3D coordinate, as shown in Fig. 3. A point feature $i \in P$ can be extracted from different sensors by measuring it in the local frame,

$$\mathbf{z}_i = h_i(\mathbf{x}_I, \mathbf{x}_i) + \boldsymbol{\nu}_i = {}^I_G \mathbf{R}({}^G \mathbf{p}_i - {}^G \mathbf{p}_I) + \boldsymbol{\nu}_i, \quad (9)$$

where ${}^G \mathbf{p}_i \in \mathbb{R}^3$ and ${}^G \mathbf{p}_I \in \mathbb{R}^3$ are the 3D positions of the point feature and the local vehicle in the global frame. $\boldsymbol{\nu}_i \in \mathbb{R}^3$ is the measurement noise. ${}^I_G \mathbf{R} \in \text{SO}(3)$ represents the rotation from the local frame to the global frame. By defining the state of point feature as $\mathbf{x}_i = {}^G \mathbf{p}_i$, we have the Jacobians calculated in Appendix A-A.

B. Line Feature

One most commonly implemented representation of a line feature in 3D space is its Plücker coordinates. For an infinite line $j \in L$, its Plücker coordinates are defined as $\mathbf{l}_j \triangleq [\mathbf{n}_j^\top \ \mathbf{v}_j^\top]^\top$, \mathbf{n}_j and \mathbf{v}_j are the normal vector and directional

vector calculated from any two distinct points on the line, as shown in Fig. 3.

A measurement of an infinite line can be modeled as its Plücker coordinates in the local frame as

$$\begin{aligned} \mathbf{z}_j &= {}^I \mathbf{l}_j = h_j({}^G \mathbf{x}_I, {}^G \mathbf{l}_j) + \boldsymbol{\nu}_j \\ &= \begin{bmatrix} {}^I_G \mathbf{R} & -{}^I_G \mathbf{R} [{}^G \mathbf{p}_I]_\times \\ \mathbf{0}_3 & {}^I_G \mathbf{R} \end{bmatrix} {}^G \mathbf{l}_j + \boldsymbol{\nu}_j, \end{aligned} \quad (10)$$

where $\boldsymbol{\nu}_j \in \mathbb{R}^6$ is the measurement noise.

Obviously, the expression \mathbf{l}_j is not a minimum parameterization of the line state. To calculate the Jacobian, here we implement the closest point approach described in [35], which is formulated as $\mathbf{p}_j = d_j \bar{\mathbf{q}}_j \in \mathbb{R}^4$, where the unit quaternion $\bar{\mathbf{q}}_j$ and the closest distance of the line to the origin can be calculated from the Plücker coordinates respectively as

$$\mathbf{R}_j(\bar{\mathbf{q}}_j) = \begin{bmatrix} \frac{\mathbf{n}_j}{\|\mathbf{n}_j\|} & \frac{\mathbf{v}_j}{\|\mathbf{v}_j\|} & \frac{\mathbf{n}_j}{\|\mathbf{n}_j\|} \times \frac{\mathbf{v}_j}{\|\mathbf{v}_j\|} \end{bmatrix}, \quad (11)$$

$$d_j = \frac{\|\mathbf{n}_j\|}{\|\mathbf{v}_j\|}, \quad (12)$$

where $\mathbf{R}_j(\bar{\mathbf{q}}_j)$ is the corresponding rotation matrix to $\bar{\mathbf{q}}_j$. By defining the line state as $\mathbf{x}_j = {}^G \mathbf{p}_j$, we have a minimum parameterization of the line in Euclidean space. The corresponding measurement Jacobians is provided in Appendix A-B.

C. Plane Feature

An infinite plane $k \in \Pi$ can be minimally parameterized by the closest point $\mathbf{p}_k = d_k \mathbf{n}_k \in \mathbb{R}^3$, as shown in Fig. 3, where \mathbf{n}_k is the plane's unit normal vector, and d_k is the distance from the origin to the plane. The plane measurement here is modeled as the closest point in the local frame as

$$\mathbf{z}_k = {}^I \mathbf{p}_k + \boldsymbol{\nu}_k = {}^I \mathbf{n}_k d_k + \boldsymbol{\nu}_k, \quad (13)$$

where $\boldsymbol{\nu}_k \in \mathbb{R}^3$ represents the plane measurement noise. The translation of the unit normal vector and distance of a plane from the global frame to the local frame is

$$\begin{bmatrix} {}^I \mathbf{n}_\pi \\ {}^I d_\pi \end{bmatrix} = \begin{bmatrix} {}^I_G \mathbf{R} & \mathbf{0}_{3 \times 1} \\ -{}^I_G \mathbf{p}_I^\top & 1 \end{bmatrix} \begin{bmatrix} {}^G \mathbf{n}_\pi \\ {}^G d_\pi \end{bmatrix}. \quad (14)$$

Incorporating (14) into (13), the plane measurement can be expressed with the normal vector ${}^G \mathbf{p}_I^\top$ and distance ${}^G d_\pi$ in the global frame as

$$\begin{aligned} \mathbf{z}_k &= {}^I d_k {}^I \mathbf{n}_k + \boldsymbol{\nu}_k = (-{}^G \mathbf{p}_I^\top {}^G \mathbf{n}_k + {}^G d_k) {}^I_G \mathbf{R} {}^G \mathbf{n}_k + \boldsymbol{\nu}_k \\ &= -{}^G \mathbf{n}_k^\top {}^G \mathbf{p}_I {}^I_G \mathbf{R} {}^G \mathbf{n}_k + {}^G d_k {}^I_G \mathbf{R} {}^G \mathbf{n}_k + \boldsymbol{\nu}_k. \end{aligned} \quad (15)$$

Define the state of a plane k as $\mathbf{x}_k = {}^G \mathbf{p}_k = {}^G d_k {}^G \mathbf{n}_k$, we can calculate the measurement Jacobians in Appendix A-C.

Remark 2. In our paper, the raw sensor measurement models of different geometric features are not explicitly provided since they are highly dependent on the sensing mechanism of different sensors. Our purpose here is to provide a common framework implementing the heterogeneous features rather than considering a specific sensor.

V. STRUCTURE PRIORS FORMULATION

In this part, the structural priors are formulated as the relative relationships between features. Specifically, the angles and distances are defined between different geometric primitives, including point, line, and plane.

A. Feature-to-Feature Prior Modeling

The structure prior factors are plotted as blue edges in the factor graph, as shown in Fig. 2. Denote the topology set containing all the pairwise structural priors as \mathcal{S} , then an edge $(i, j) \in \mathcal{S}$ indicates that some quantitative measurements between two features $a, b \in \{P, L, \Pi\}$, denoted as \mathbf{z}_{ab} , are known a priori. Let h_{ab} denotes the measurement function between a, b , the structural prior residual can be obtained as

$$\mathbf{r}_{ab} = h_{ab}(\hat{\mathbf{x}}_a, \hat{\mathbf{x}}_b) - \mathbf{z}_{ab}. \quad (16)$$

The residual cost term is

$$\sum_{(a,b) \in \mathcal{S}} \|\mathbf{r}_{ab}\|_{\Sigma_{ab}}^2, \quad (17)$$

where Σ_{ab} is the covariance of the measurement noise which represents the fidelity of implementing specific structural prior constraints. The following are to model the pairwise measurements between point, line, and plane features described above.

B. Feature-to-Feature Factors

1) *Point-to-Point Factor*: When two salient points are detected, the possible structure prior information that characterizes the spatial relationship can be modeled as a 1-3 dimensional measurement. Denote two point features $i, i' \in P$, and their relative translation $\mathbf{x}_{ii'} = \mathbf{x}_{i'} - \mathbf{x}_i$, the point-to-point structural measurement

$$\mathbf{z}_{ii'} = h_{ii'}(\mathbf{x}_{ii'}) \quad (18)$$

is to project the 3D displacement between the two points onto a specific 1-3D metric in the global frame. Specifically, the distance measurement can be modeled as $z_{ii'}^d = \|\mathbf{x}_{ii'}\|$.

The measurement residual Jacobians with respect to the points state are provided in Appendix B-A.

Remark 3. In the point-to-point structure, the points should be salient in both texture and structure senses. In practice, most points are distributed according to the texture, and it may not be easy to endow structural information. Some examples of structurally salient points are intersection points, endpoints, and corner points. The integration of point-to-point structural prior information depends on the extraction and recognition of structural points, which may be challenging in practice.

2) *Point-to-Line Factor*: The spatial relationship between a point and an infinite line can be described with a 2D vector. With a point $i \in P$ and a line $j \in L$, we define a 2D displacement between them as

$$\mathbf{x}_{ij} = \begin{bmatrix} \bar{\mathbf{n}}_j^\top \\ \bar{\mathbf{n}}_j^\top \times \bar{\mathbf{v}}_j^\top \end{bmatrix} \mathbf{x}_i + \begin{bmatrix} 0 \\ d_j \end{bmatrix} \in \mathbb{R}^2, \quad (19)$$

where $\bar{\mathbf{n}}_j = \frac{\mathbf{n}_j}{\|\mathbf{n}_j\|}$, $\bar{\mathbf{v}}_j = \frac{\mathbf{v}_j}{\|\mathbf{v}_j\|}$, and d_j are the line j 's unit normal vector, unit directional vector, and the distance

to the origin point, respectively. Denote the point-to-line measurement of \mathbf{x}_{ij} as

$$\mathbf{z}_{ij} = h_{ij}(\mathbf{x}_{ij}), \quad (20)$$

when $h_{ij}(\cdot)$ is a norm operator, $z_{ij}^d = h_{ij}(\mathbf{x}_{ij})$ measures the minimum distance from a point i to a line j . Hereafter, the point-on-line constraint can be enforced by $z_{ij}^d = 0$. The measurement residual Jacobian is calculated as Appendix B-B.

3) *Point-to-Plane Factor*: The relationship between a point and an infinite plane can be described with one scalar, i.e., the distance from the point to the plane. With a point feature $i \in P$, and an infinite plane feature $k \in \Pi$, the distance between a point and a plane is defined as

$$d_{ik} = (\mathbf{n})^\top \mathbf{p}_i + d_k. \quad (21)$$

Define a measurement function as $z_{ik} = d_{ik}$, then the point-on-plane constraint can be enforced by letting $z_{ik} = 0$. The measurement residual Jacobian is provided in Appendix B-C.

4) *Line-to-Line Factor*: The relationship of two lines can be uniquely parameterized with a 3D translation vector and a rotation angle. Given two lines, denoted respectively as $j, j' \in L$, the rotation $\alpha_{jj'}$ and translation $\mathbf{d}_{jj'} \in \mathbb{R}^3$ can be calculated as follows:

$$\alpha_{jj'} = \mathbf{v}_j^\top \mathbf{v}_{j'}, \quad (22)$$

and

$$\mathbf{d}_{jj'} = \begin{cases} \mathbf{0}, & j \text{ and } j' \text{ intersection,} \\ \bar{\mathbf{d}}_{jj'}, & j \text{ and } j' \text{ are parallel,} \\ (\bar{\mathbf{v}}_j \times \bar{\mathbf{v}}_{j'})^\top \bar{\mathbf{d}}_{jj'} (\bar{\mathbf{v}}_j \times \bar{\mathbf{v}}_{j'}), & \text{otherwise,} \end{cases} \quad (23)$$

where $\bar{\mathbf{d}}_{jj'} = d_j \bar{\mathbf{n}}_j \times \bar{\mathbf{v}}_j - d_{j'} \bar{\mathbf{n}}_{j'} \times \bar{\mathbf{v}}_{j'}$. We first consider the rotation $\alpha_{jj'}$ as a measurement between two lines. Further, when two lines are parallel, namely $\alpha_{jj'} = \pm 1$, the distance $d_{jj'} = \|\mathbf{d}_{jj'}\|$ is considered as another measurement, namely

$$\mathbf{z}_{jj'} = \begin{cases} \begin{bmatrix} \alpha_{jj'} & d_{jj'} \end{bmatrix}^\top, & \text{in parallel,} \\ \alpha_{jj'}, & \text{otherwise.} \end{cases} \quad (24)$$

The Jacobian of line-line measurement residual is provided in B-D.

5) *Line-Plane Factor*: The spatial relationship between a line and a plane can be characterized by the dot product of the directional vector of a line $j \in L$ and the normal vector of a plane $k \in \Pi$, denoted as α_{jk} :

$$\alpha_{jk} = \bar{\mathbf{v}}_j^\top \mathbf{n}_k. \quad (25)$$

Especially, when $\alpha_{jk} = 0$, namely a line is parallel to a plane, a distance can further calculated as

$$d_{jk} = \mathbf{n}_k^\top (\bar{\mathbf{n}}_j \times \bar{\mathbf{v}}_j) d_j - d_k. \quad (26)$$

The measurement therefore is

$$\mathbf{z}_{jk} = \begin{cases} \begin{bmatrix} \alpha_{jk} & d_{jk} \end{bmatrix}^\top, & \text{in parallel,} \\ \alpha_{jk}, & \text{otherwise.} \end{cases} \quad (27)$$

Specifically, the line-on-plane constraint is enforced as $\alpha_{jk} = 0$, and $d_{jk} = 0$. The associated Jacobian is provided in Appendix B-E.

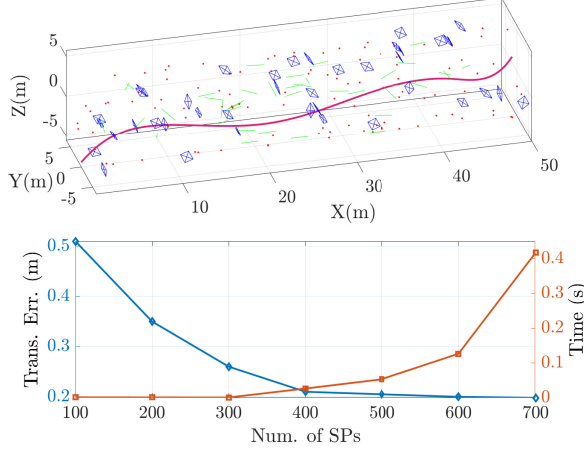


Fig. 4: The translational estimation error and calculation time as number of SP grows.

6) *Plane-to-Plane Factor*: Similar to the above formulations, a similar dot product between the unit normal vectors of two planes, can be calculated as

$$\alpha_{kk'} = \mathbf{n}_k^\top \mathbf{n}_{k'}. \quad (28)$$

When two planes are parallel, the displacement can also be calculated as

$$\mathbf{d}_{kk'} = \mathbf{x}_{k'} - \mathbf{x}_k = \mathbf{n}_k(d_{k'} - d_k) = \mathbf{n}_{k'}(d_{k'} - d_k). \quad (29)$$

Define the measurement of the relationship as

$$\mathbf{z}_{jk} = \begin{cases} [\alpha_{kk'} & d_{kk'}]^\top, & k \text{ parallel to } k', \\ \alpha_{kk'}, & \text{otherwise.} \end{cases} \quad (30)$$

The measurement Jacobians are provided in Appendix B-F.

With the above formulation of spatial relationships between features, the structure priors can be encoded into low dimensional angles and/or distances. The low dimensional encoding makes their associations with the structure priors database easy. Both the heterogeneous geometric feature factors and the structure prior factors are further integrated with the graph optimization toolbox GTSAM [11].

VI. STRUCTURE PRIOR SELECTION

According to the above formulations of the structure information between features, there are at most $n(n-1)/2$ possible feature priors in a scenario with n geometric features. In the graph optimization process, incorporating too many structure priors will severely damage the sparsity of the graph matrix, therefore will slow down the optimization. As an illustrative example, a synthetic environment with 100 points, 40 lines, and 40 planes are shown in Fig. 4. Despite the localization error decreases as more structural priors are incorporated into the optimization, the optimization efficiency deteriorates simultaneously. Among all the potential prior information, some are not as helpful as others, and there may also exist redundancies in the structure priors set. Therefore, it is meaningful to develop a strategy to select the most useful structure

priors to incorporate in the optimization, which is formulated as Problem 1 as follows.

Problem 1. Let \mathcal{S} be a finite set of the structure priors, and $f : 2^{|\mathcal{S}|} \rightarrow \mathbb{R}$ be a real value function representing a measure of information obtained. Then the feature selection strategy is to obtain a most informative subset $X \subseteq \mathcal{S}$ that maximizes f :

$$\max_{X \subseteq \mathcal{S}} f(X) \text{ s.t. } |X| \leq N. \quad (31)$$

Apparently, Problem 1 is NP-hard and the optimal solution can not be found efficiently.

In this paper, we consider implementing the Fisher Information Matrix (FIM) to measure the contribution of a structure prior to the localization performance. Denote the belief of the state within the sliding window of time t as $\mathcal{X}_t \sim \mathcal{N}(\bar{\mathcal{X}}_t, \mathbf{P}_t)$, and one structural prior $s \in \mathcal{S}$ of current local map as a measurement, $h_s(\mathcal{X}_t) \sim \mathcal{N}(\mathbf{z}_s, \Sigma_s)$, we have the following equation according to the Bayes' rule

$$\mathbf{P}_{t+}^{-1} = \mathbf{P}_t^{-1} + \sum_{s \in \mathcal{S}_t} \mathbf{I}_s, \quad (32)$$

where $\mathbf{I}_s = \mathbf{J}_s^T \Sigma_s^{-1} \mathbf{J}_s$ is the FIM of a specific feature s . \mathbf{J}_s is the Jacobian of the structure prior s with regard to the local pose. \mathbf{P}_t and \mathbf{P}_{t+} denote the covariance before and after integrating the structure priors, respectively.

Further the informativeness measure function f is defined using the D-optimal criteria similar to [44], and provided as below.

$$\begin{aligned} f(X) &= \log \det (\mathbf{A} \mathbf{P}_{t+}^{-1} \mathbf{A}^\top) \\ &= \log \det \left(\mathbf{A} (\mathbf{P}_t^{-1} + \sum_{s \in \mathcal{S}_t} \mathbf{I}_s) \mathbf{A}^\top \right). \end{aligned} \quad (33)$$

By maximizing the f function, the minimization of interest state, which is selected by the matrix \mathbf{A} , can be achieved in the D-optimal fashion.

With the definition of the scalar function f , we have the following Lemma 1.

Lemma 1. The scalar function $f : 2^{|\mathcal{S}|} \rightarrow \mathbb{R}$ is monotone and submodular w.r.t to the feature set X , namely, given the subsets $X_1 \subset X_2 \subset \mathcal{S}$, for each $s \in \mathcal{S} \setminus X_2$, the following in-equation holds:

$$f(X_1 \cup \{s\}) - f(X_1) \geq f(X_2 \cup \{s\}) - f(X_2). \quad (34)$$

Proof. The proof is similar to the results provided in [45] and omitted here. \square

With the submodularity property of the informativeness measure function, Problem 1, although NP-hard, can be solved approximately with guaranteed optimality. In this paper, we implement a stochastic greedy algorithm with the lazy evaluation as Algorithm 1. In the outer stochastic greedy loop, during each iteration, we select one most informative feature from a subset of candidate features with size N . The inner lazy evaluation is to speed up the searching with a upperBound(\cdot) function, which is to calculate the upper bound of the $\log \det(\cdot)$ function of a positive definite matrix using the Hadamard's in-equality [46].

Algorithm 1: Stochastic Greedy Algorithm with Lazy Evaluation

Input: $f : 2^{\mathcal{S}} \rightarrow \mathbb{R}, \mathcal{S}$.
Output: A subset $X \subset \mathcal{S}$ satisfying $|X| = N$.
 $X \leftarrow \emptyset$;
for $i \leftarrow 1; i \leq N; i \leftarrow i + 1$ **do**
 $R \leftarrow$ a random subset by sampling n random elements from $\mathcal{S} \setminus X$;
 $[U_1, U_2, \dots, U_n] \leftarrow \text{upperBounds}(X \cup j), j = 1, \dots, n$;
 $\mathbf{U} \downarrow \leftarrow \text{sort}(U_1, \dots, U_n)$;
 $f_{\max} = -1, l_{\max} = -1$;
 for $l \in \mathbf{U} \downarrow$ **do**
 if $U_l < f_{\max}$ **then**
 break;
 end
 if $f(X \cup l) > f_{\max}$ **then**
 $f_{\max} = f(X \cup l), l_{\max} = l$
 end
 end
 $X \leftarrow X \cup l_{\max}$;
end

Based on Algorithm 1, a subset of \mathcal{S} , although not optimal, can be obtained with guaranteed optimality property and much cheaper computation cost, which is quantitatively provided as below.

Proposition 1. (Approximated Optimality Guarantee. [47] Theorem 1). *Let f be a non-negative monotone submodular function. Let us also set sampling set $n = \frac{|\mathcal{S}|}{N} \log \frac{1}{\epsilon}$. Then the stochastic greedy achieves a $(1 - \frac{1}{e} - \epsilon)$ approximation guarantee in expectation to the optimum solution of Problem 1 with only $O(n \log \frac{1}{\epsilon})$ computation cost.*

VII. EXPERIMENT EVALUATION

In this part, the proposed SPINS is tested based on synthetic data, the public datasets, and, most importantly, on real flight data that is collected with a UAV during a building inspection task.

A. Synthetic data

To evaluate the localization performance of the proposed framework, we create a customized 2.5D indoor simulation scenario with a size $28\text{m} \times 16\text{m} \times 3\text{m}$. The point, line, and plane features are placed as presented in Fig. 5. A 3D robot trajectory is generated within the simulation space based on spline functions and plotted in Fig. 5 as a red curve. The orientation of the robot's body frame is also plotted periodically. In order to evaluate the proposed SPINS framework, we also simulate data of both interoceptive measurement of local robot and exteroceptive measurement of the environment. Specifically, an IMU is simulated by adding noise to the groundtruth robot states, which are obtained from the differentiation of the 3D spline trajectory, and the noise is generated and added according to the ADIS16448

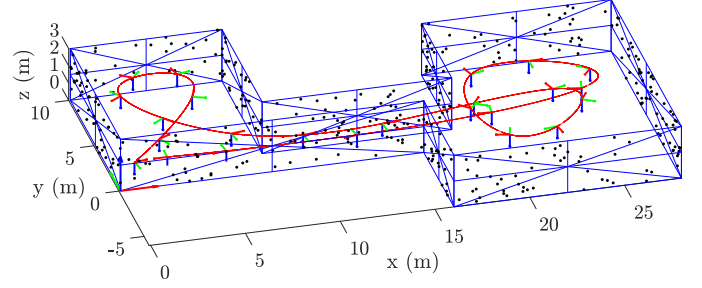


Fig. 5: The simulated 2.5D indoor scenario. The robot trajectory is drawn in red curve with the coordinate of the robot pose. The feature points and lines are plotted on planes.

TABLE I: Sensor Parameters

Sensory Parameters	Value
IMU Gyroscope Noise Density	0.005 rad/s $\sqrt{\text{Hz}}$
IMU Gyroscope Random Walk	4.0e-6 rad/s $^2\sqrt{\text{Hz}}$
IMU Accelerometer Noise Density	0.001 m/s $^2\sqrt{\text{Hz}}$
IMU Accelerometer Random Walk	2.0e-4 m/s $^3\sqrt{\text{Hz}}$
Point Feature Measurement	$\Sigma_i = 0.02\mathbf{I}_3\text{m}^2$
Line Feature Measurement	$\Sigma_j = 0.01\mathbf{I}_6\text{m}^2$
Plane Feature Measurement	$\Sigma_k = 0.01\mathbf{I}_3\text{m}^2$
Sensor Rate	30Hz
Sensor FOV	120 $^\circ \times 90^\circ$

IMU sensor specifications listed in [32]. To simplify the perception process, we haven't explicitly simulated the raw data of a specific sensor, and instead, we assume that the 3D geometry information of the features is obtained according to the measurement function described in Section IV with extra FOV limitations. The overall sensory parameters are list as Table I.

The factor graph of the simulation is built with a modified version of the GTSAM package¹, which we additionally integrates the line and plane factors, and the structure prior factors. The sliding window based optimization is solved based on its iSAM2 solver. 100 Monte-Carlo simulations are carried out based on point, line and plane features and different structure priors configurations to investigate the performance of the proposed framework. Specifically, we consider 3 feature combinations, which are 1) point feature (P-INS), 2) point and line features (PL-INS), 3) point, line, and plane features (PLP-INS), and our SPINS. Moreover, our SPINS further incorporates structure priors based on 4 different strategies, which are 1) selecting 20 structure priors in each sensory data frame randomly (SPINS-Rand. 20 SP), 2) selecting the most informative 20 structure priors according to Algorithm 1 (SPINS-App. Info. Opt. 20 SP), 3) selecting the most informative 20 structure priors exhaustively (SPINS-Info. Opt. 20 SP) and 4) selecting all structure priors (SPINS-All SP). The structures information listed as Table II are extracted from the ground truth map and implemented according to different strategies.

The root-mean-square errors (RMSEs) of translational and rotational estimates are plotted in Fig. 6. The complete quantitative comparison between different strategies is also provided

¹<https://github.com/borglab/gtsam.git>

TABLE II: Structure Priors between Features.

	Line	Plane
Point	Points on the Line	Points on the Plane
Line	-Parallelism with distance -Orthogonality	-Orthogonality -Parallelism with distance -Line on the Plane
Plane	-	-Parallelism with distance -Orthogonality

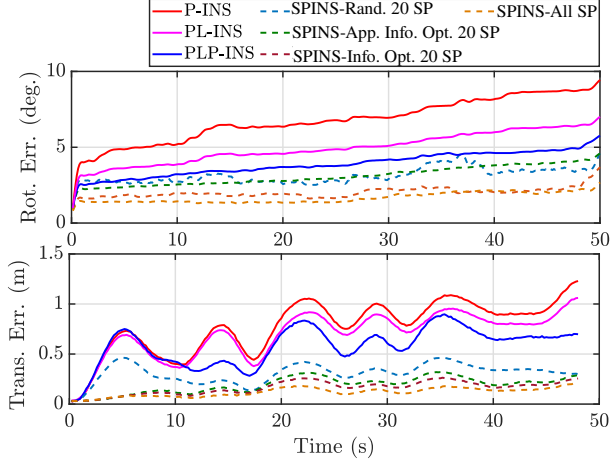


Fig. 6: The translational and rotational RMSE under different feature and structure priors configurations.

in Tab. II. The localization results of using heterogeneous features without structure prior information are plotted as solid lines in different colors. It is apparent that more accurate translational and rotational estimation results can be obtained as more types of features are implemented. Moreover, the integration of structure prior information can further improve the localization performance, as the translational and rotational errors plotted in dashed lines indicated. Specifically, integrating all structure prior information can unsurprisingly achieve the best localization performance. Nevertheless, the computation time for solving each round of the local optimization also significantly increases, as provided in Tab. II. With the same amount of 20 structure priors integrated, the optimal solution, by choosing the most informative combination of 20 structure priors, achieves the closest result to the method with all structure priors. However, the exhausted searching takes too much time. Our proposed method in Algorithm 1, although not as good as the exhausted searching method, can achieve comparable results to that, but with much less search effort. Conclusively, Our proposed method may be a potential strategy in real-time applications.

B. Euroc Dataset

In this part, the proposed SPINS framework is tested on the public Euroc MAV Dataset [43]. We implement the sashago front-end package² to deal with the feature detection and tracking of point, line, and plane features. We extracted planes from the ground truth point cloud of the vicon room to calculate the structural priors, as shown in Fig. 7. The distributions of

TABLE III: Average RMSE over Mento-Carlo simulations with different strategies.

Strategies	Trans. Errors [m]	Rot. Errors [deg.]	Time per iteration [s]
P-INS	0.8186	6.9399	0.0180
PL-INS	0.6103	5.0499	0.0193
PLP-INS	0.4863	3.9595	0.0274
SPINS-Rand. 20 SPs	0.3242	3.1684	0.0259
SPINS-App. Opt. 20 SPs	0.2082	3.1652	0.0301
SPINS-Opt. 20 SPs	0.1757	2.0399	0.3175
SPINS-All SPs	0.1277	1.6984	0.2463

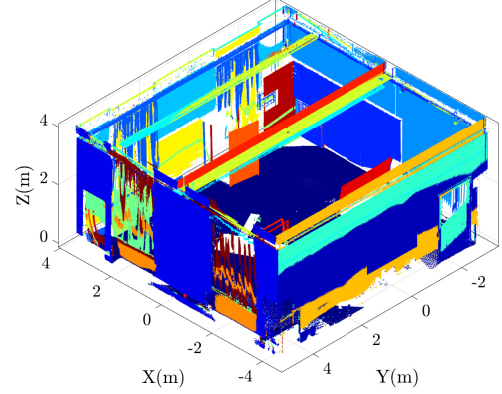


Fig. 7: The structural priors extracted from the ground-truth scan of the vicon room.

angles between planes and the distances of parallel planes are plotted in Fig. 8, which show the repetition and sparsity angle and distance pattern in a man-made environment. The point-on-plane, line-on-plane, and plane-plane angles and distances are treated as structure priors and further integrated into the estimation.

The localization results by implementing the VINS FUSION³, ORB-SLAM3⁴, the heterogeneous features based method [35], and the proposed framework are listed in Table IV based on the evaluation method described in [48]. As indicated, our proposed method can achieve the best performance in both translational and rotational RMSE in V1_01, V2_01, V2_02 and V2_03. Specifically, our proposed SPINS outperforms the PLP based method [35] in all datasets, which shows the effectiveness of incorporating the structure prior information. The advantage of using heterogeneous features in the localization is not well supported in the datasets due to the point feature richness are enhanced on purpose, and therefore the complementary effect of the line and plane is not obvious.

As one example, the results of estimated trajectories of V2_02 are plotted in Fig. 9.

²https://gitlab.com/srrg-software/srrg_sashago

³<https://github.com/HKUST-Aerial-Robotics/VINS-Fusion.git>

⁴https://github.com/UZ-SLAMLab/ORB_SLAM3.git

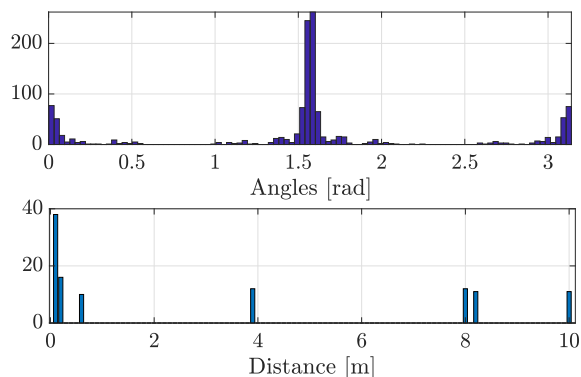


Fig. 8: The angles and distances distribution of segmented planes in Fig.7

TABLE IV: The RMSE of the estimation results based on different methods

Data	Trans. RMSE [m]/Rot. RMSE [°]			
	VINS	ORB3	PLP	SPINS
V1_01	0.129/1.748	0.085/1.484	0.098/1.674	0.079/1.131
V1_02	0.145/1.504	0.089/1.336	0.321/1.455	0.094/0.905
V1_03	0.144/1.967	0.093/1.952	0.193/2.389	0.095/1.762
V2_01	0.150/3.121	0.085/1.852	0.116/2.352	0.077/1.731
V2_02	0.197/4.413	0.167/3.141	0.188/4.581	0.160/3.030
V2_03	0.219/2.924	0.160/3.007	0.213/3.458	0.151/2.988

C. Inspection Data

In this part, the proposed SPINS is further tested on a real civilian application scenario. A DJI M600 pro hexacopter is utilized in a building inspection task by following a specific trajectory covering the façade of the building, as presented in Fig. 10. Navigating a robot in such an application is challenging if no highly reliable positioning information is available. Usually, the GPS signal may not provide reliable positioning information due to interference or obstruction nearby a building. Moreover, the localization method by measuring the building may also not work well due to low feature density and repetitive façade patterns. As presented in Fig. 10, the building can be approximately treated as a 2.5D object, which does not have much structural variation in the z direction

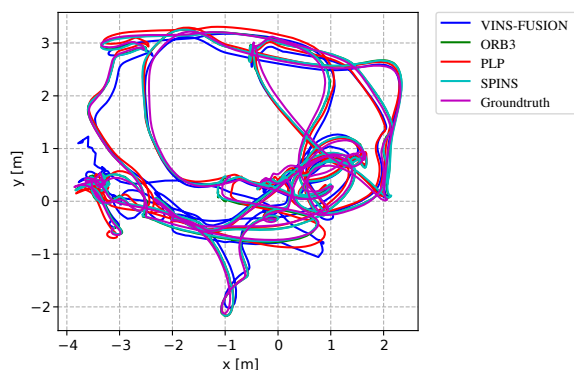


Fig. 9: The estimated trajectories of V1_03 based on the VINS-FUSION, ORB3 and the proposed SPINS with PLP and PLP-SP setups.

TABLE V: Typical distance value for a building

Distance Type	Typical Value [m]
Parallel Lines	[0.3, 0.5, 1.2, 1.5, 2.5, 3.3, 4]
Parallel Line to Plane	[0.5, 1.2, 2.7, 3, 4]
Parallel Planes	[1.5, 3, 4.5, 6]

and plenty planar features in x and y directions. Worse still, the façade of the building may not contain sufficient textural points, and most of the point and line features are located on structural boundaries.

To guarantee the quality and safety of the inspection task, we developed an on-board navigation system including multiple sensors to collect real time environment sensing data, as shown in Fig. 10. The proposed SPINS method is further tested on this data. Specifically, we utilize the forward-looking stereo vision cameras to obtain point and line features on the building façade, and the horizontal mounted LiDAR to measure the planes. The one shot features extraction example is shown in Fig. 11. Similar structural priors as list in Table I are adopted. We select some typical distances which are treated as the main distance patterns in the building, as listed in Table V. To evaluate the performance of the proposed method, a Leica Geosystem that measures the visual anchor with millimeter accuracy is adopted to provide the groundtruth of 3D location.

The proposed algorithm, along with the VINS-FUSION and ALOAM, is tested based on the recorded data on a laptop with Intel i7-8550U CPU and 16 GB memory. The localization results of the inspection using different methods are presented from Fig. 12 to Fig. 14. The trajectories of different localization methods along with the groundtruth (GT) are plotted in Fig. 12, although all trajectories are initialized at the same $[0, 0, 0]^T$, the trajectories from the VINS drifts as time goes on. Specifically, from Fig. 13, it's clear that the trajectories from VINS drifts in x and y directions due to the low feature density and variation during the horizontal movement, and on the other hand, the trajectory from ALOAM drifts mainly in the z direction due to low depth variation during vertical movement in z direction movement in a 2.5D building. As indicated in Fig. 14, the results obtained by using point, line and plane features apparently have better performance in all three directions. Moreover, the integration of structural priors (PLP-SP) outperformed the PLP method with the provide structure prior information. The position estimation RMSE of the PLP and SPINS are 1.018m and 0.7452m, respectively, with a significant position accuracy improvement by incorporating the structure priors.

VIII. CONCLUSIONS

We propose a sliding window optimization-based localization framework utilizing point, line, and plane features. Considering heterogeneous features, we further develop a structure priors integration method that can further improve localization robustness and accuracy. To alleviate the computation burden brought by extra structure factor edges in the factor graph, we adopt a screening mechanism to select the most informative structure priors. The advantages of the

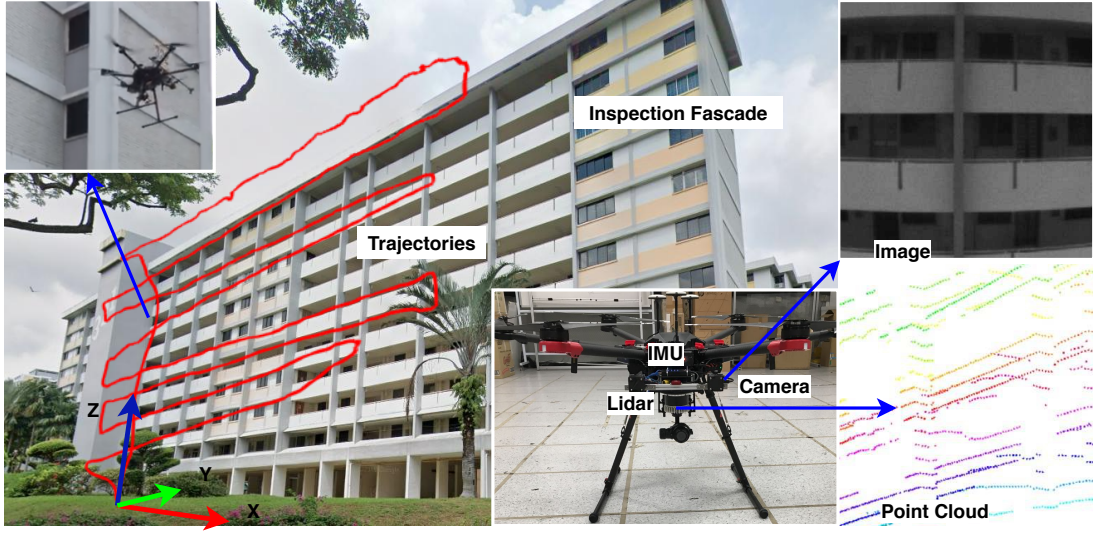


Fig. 10: The building inspection task using a DJI M600 hexacopter with onboard cameras, Lidars, and IMUs.

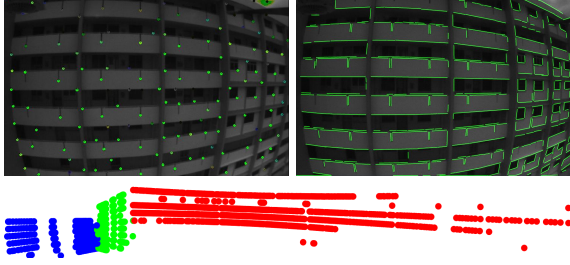


Fig. 11: The extraction of point, line and plane features from both vision and LiDAR.

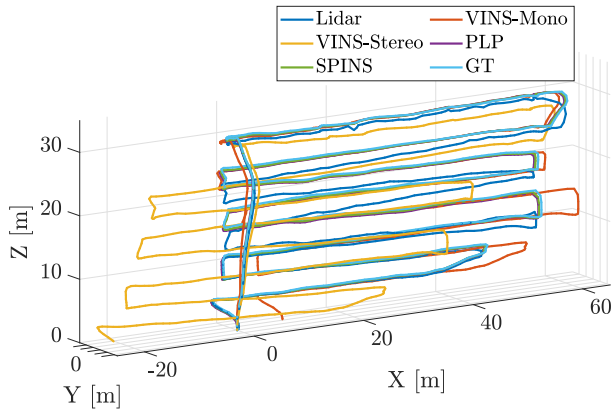


Fig. 12: The estimated trajectories from different methods.

proposed frameworks are demonstrated extensively based on synthetic data, public datasets, and a real flight dataset obtained from a building inspection mission. In the future, we will further investigate improving the performance of the front-end, namely the feature detection and tracking process, to enable the framework validated on a robot platform with limited computation capacity.

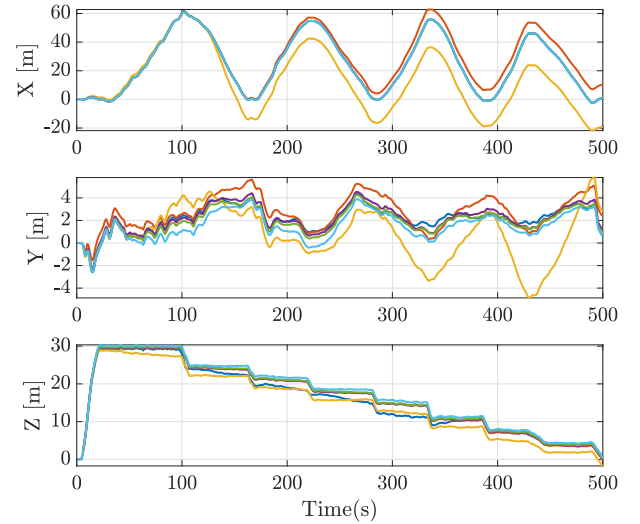


Fig. 13: The estimation on X,Y,Z directions.

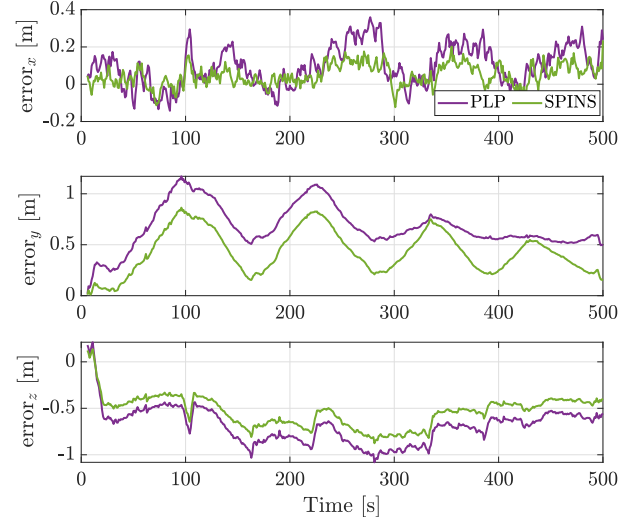


Fig. 14: The localization errors on X,Y,Z directions.

APPENDIX A
JACOBIANS OF HETEROGENEOUS FEATURE
MEASUREMENTS

A. Point Measurement Jacobians

The Jacobians, according to the formulations in (5), are related to the state of the point in Euclidean space $\mathbf{x}_i = {}^G\mathbf{p}_i$, and the pose of the robot in SE(3), and can be calculated as follows.

$$\mathbf{J}_{\hat{\mathbf{x}}_i}^{\mathbf{r}_i} = \frac{\partial \mathbf{r}_i(\hat{\mathbf{x}}_i + \Delta \mathbf{x}_i)}{\partial \Delta \mathbf{x}_i} \Big|_{\Delta \mathbf{x}_i=0} = {}^I_G \hat{\mathbf{R}}, \quad (35)$$

and

$$\begin{aligned} \mathbf{J}_{\hat{\mathbf{p}}_I}^{\mathbf{r}_i} &= \frac{\partial \mathbf{r}_i(\hat{\mathbf{x}}_I \boxplus \Delta \mathbf{x}_I)}{\partial \delta \mathbf{p}_I} \Big|_{\Delta \mathbf{x}_I=0} = -{}^I_G \hat{\mathbf{R}}, \\ \mathbf{J}_{\hat{\mathbf{q}}_I}^{\mathbf{r}_i} &= \frac{\partial \mathbf{r}_i(\hat{\mathbf{x}}_I \boxplus \Delta \mathbf{x}_I)}{\partial \delta \boldsymbol{\theta}_I} \Big|_{\Delta \mathbf{x}_I=0} = -{}^I_G \hat{\mathbf{R}}[\hat{\mathbf{p}}_I]_{\times}, \end{aligned} \quad (36)$$

where $\Delta \mathbf{x}_i$ and $\Delta \mathbf{x}_I$ are the perturbations on $\hat{\mathbf{x}}_i$ and $\hat{\mathbf{x}}_I$, respectively. Specifically, $[\delta \boldsymbol{\theta}_I^\top, \delta \mathbf{p}_I^\top]^\top$ are the rotational and translational part of the perturbation $\Delta \mathbf{x}_I$. The measurement Jacobians over other parts of \mathbf{x}_I are $\mathbf{0}$.

B. Line Measurement Jacobians

The measurement residual Jacobian w.r.t the local pose is

$$\begin{aligned} \mathbf{J}_{\hat{\mathbf{q}}_I}^{\mathbf{r}_j} &= \frac{\partial \mathbf{r}_j(\hat{\mathbf{x}}_I \boxplus \Delta \mathbf{x}_I)}{\partial \delta \boldsymbol{\theta}_I} \Big|_{\Delta \mathbf{x}_I=0} \\ &= \begin{bmatrix} [{}^I_G \hat{\mathbf{R}} \hat{\mathbf{n}}_j]_{\times} - [{}^I_G \hat{\mathbf{R}} [{}^G \hat{\mathbf{p}}_I]_{\times} {}^G \hat{\mathbf{v}}_j]_{\times} \\ - [{}^I_G \hat{\mathbf{R}} {}^G \hat{\mathbf{v}}_j]_{\times} \end{bmatrix}, \\ \mathbf{J}_{\hat{\mathbf{p}}_I}^{\mathbf{r}_j} &\doteq \frac{\partial \mathbf{r}_j(\hat{\mathbf{x}}_I \boxplus \Delta \mathbf{x}_I)}{\partial \delta \mathbf{p}_I} \Big|_{\Delta \mathbf{x}_I=0} \\ &= \begin{bmatrix} {}^I_G \hat{\mathbf{R}} [{}^G \hat{\mathbf{v}}_j]_{\times} \\ \mathbf{0}_3 \end{bmatrix}. \end{aligned} \quad (37)$$

The measurement residual Jacobians w.r.t. to line state can be calculated using the chain rule as

$$\mathbf{J}_{\hat{\mathbf{x}}_j}^{\mathbf{r}_j} = \mathbf{J}_{\bar{\mathbf{l}}_j}^{\mathbf{r}_j} \mathbf{J}_{\hat{\mathbf{x}}_j}^{\bar{\mathbf{l}}_j}, \quad (38)$$

where $\bar{\mathbf{l}}_j = [\bar{\mathbf{q}}_j^\top \ d_j]^\top$ is an intermediate state. Specifically, with perturbation $\delta \bar{\mathbf{l}}_j = [\delta \boldsymbol{\theta}_j^\top \ \delta d_j]^\top$ on manifold $\bar{\mathbf{l}}_j$, we have

$$\begin{aligned} \mathbf{J}_{\bar{\mathbf{l}}_j}^{\mathbf{r}_j} &= \frac{\partial \mathbf{r}_j(\hat{\mathbf{l}}_j \boxplus \delta \bar{\mathbf{l}}_j)}{\partial \delta \bar{\mathbf{l}}_j} \Big|_{\delta \bar{\mathbf{l}}_j=0} \\ &= \begin{bmatrix} {}^I_G \hat{\mathbf{R}} & -{}^I_G \hat{\mathbf{R}} [{}^G \mathbf{p}_I]_{\times} \\ \mathbf{0}_3 & {}^I_G \hat{\mathbf{R}} \end{bmatrix} \begin{bmatrix} {}^G \hat{d}_j [{}^G \hat{\mathbf{R}}_j \mathbf{e}_1]_{\times} & {}^G \hat{\mathbf{R}}_j \mathbf{e}_1 \\ [{}^G \hat{\mathbf{R}}_j \mathbf{e}_2]_{\times} & \mathbf{0}_{3 \times 1} \end{bmatrix}, \end{aligned} \quad (39)$$

and

$$\mathbf{J}_{\hat{\mathbf{x}}_j}^{\bar{\mathbf{l}}_j} = \frac{\partial \bar{\mathbf{l}}_j(\hat{\mathbf{x}}_j + \Delta \mathbf{x}_j)}{\partial \Delta \mathbf{x}_j} \Big|_{\Delta \mathbf{x}_j=0} = \begin{bmatrix} \frac{2}{d} (\hat{q}_j \mathbf{I}_3 - [\hat{\mathbf{q}}_j]_{\times}) & -\frac{2}{\hat{q}_j} \hat{\mathbf{q}}_j \\ \hat{\mathbf{q}}_j^\top & \hat{q}_j \end{bmatrix}, \quad (40)$$

where $\mathbf{e}_1, \mathbf{e}_2$ are the first and second column of the identity matrix \mathbf{I}_3 . \mathbf{q}_j and q_j are the vector part and scalar part of the quaternion $\bar{\mathbf{q}}_j$, respectively. Please refer to [28] for detailed derivation of (40).

C. Plane Measurement Jacobians

By defining an intermediate state of the plane as $\bar{\mathbf{p}}_j = [{}^G \hat{\mathbf{n}}_j^\top \ G d_k]^\top$, the measurement residual \mathbf{r}_k 's Jacobian w.r.t. the plane state $\mathbf{x}_k = {}^G \mathbf{p}_k$ can be calculated using the chain rule as

$$\mathbf{J}_{\hat{\mathbf{x}}_k}^{\mathbf{r}_k} = \mathbf{J}_{\hat{\mathbf{p}}_k}^{\mathbf{r}_k} \mathbf{J}_{\hat{\mathbf{x}}_k}^{\hat{\mathbf{p}}_k}, \quad (41)$$

where

$$\begin{aligned} \mathbf{J}_{\hat{\mathbf{p}}_k}^{\mathbf{r}_k} &= \frac{\partial \mathbf{r}_k(\hat{\mathbf{p}}_k \boxplus \delta \bar{\mathbf{p}}_k)}{\partial \delta \bar{\mathbf{p}}_k} \Big|_{\delta \bar{\mathbf{p}}_k=0} \\ &= [{}^I_G \hat{\mathbf{R}} \left(({}^G \hat{d}_k - {}^G \hat{\mathbf{n}}_k^\top {}^G \hat{\mathbf{p}}_I) \mathbf{I}_3 - {}^G \hat{\mathbf{n}}_k {}^G \hat{\mathbf{p}}_I^\top \right) \quad {}^I_G \hat{\mathbf{R}} {}^G \hat{\mathbf{n}}_k]^\top, \\ \mathbf{J}_{\hat{\mathbf{x}}_k}^{\hat{\mathbf{p}}_k} &= \frac{\partial \bar{\mathbf{p}}_k(\hat{\mathbf{x}}_k + \Delta \mathbf{x}_k)}{\partial \Delta \mathbf{x}_k} \Big|_{\Delta \mathbf{x}_k=0} = \begin{bmatrix} (\mathbf{I}_3 - {}^G \hat{\mathbf{n}}_k {}^G \hat{\mathbf{n}}_k^\top) \\ {}^G \hat{d}_k \\ {}^G \hat{\mathbf{n}}_k^\top \end{bmatrix}. \end{aligned} \quad (42)$$

$\delta \bar{\mathbf{p}}_k$ and $\Delta \mathbf{x}_k$ are perturbations on $\hat{\mathbf{p}}_k$ and $\hat{\mathbf{x}}_k$, respectively.

By injecting a small perturbation of local pose into (15), we have the measurement Jacobian w.r.t. the pose as follows:

$$\begin{aligned} \mathbf{J}_{\hat{\mathbf{q}}_I}^{\mathbf{r}_k} &= \frac{\partial \mathbf{r}_k(\hat{\mathbf{x}}_I \boxplus \Delta \mathbf{x}_I)}{\partial \delta \boldsymbol{\theta}} \Big|_{\Delta \mathbf{x}_I=0} \\ &= \left({}^G \hat{d} - {}^G \hat{\mathbf{n}}_I^\top {}^G \hat{\mathbf{p}}_I \right) [{}^I_G \hat{\mathbf{R}} {}^G \hat{\mathbf{n}}_I]_{\times}, \end{aligned} \quad (43)$$

$$\mathbf{J}_{\hat{\mathbf{p}}_I}^{\mathbf{r}_k} = \frac{\partial \mathbf{r}_k(\hat{\mathbf{x}}_I \boxplus \Delta \mathbf{x}_I)}{\partial \delta \mathbf{p}_I} \Big|_{\Delta \mathbf{x}_I=0} = -{}^I_G \hat{\mathbf{R}} {}^G \hat{\mathbf{n}}_I {}^G \hat{\mathbf{n}}_I^\top. \quad (44)$$

APPENDIX B

JACOBIANS OF THE STRUCTURAL PRIORS MEASUREMENTS

A. Point-Point Measurement Jacobians

For a pair of points $(i, i') \in \mathcal{S}$, the Jacobians of the measurement residual, defined as $\mathbf{r} = \mathbf{z} - h_{ii'}(\hat{\mathbf{x}}_i, \hat{\mathbf{x}}_{i'})$, are derived as

$$\mathbf{J}_{\hat{\mathbf{x}}_i}^{\mathbf{r}_{ii'}} = \mathbf{J}_{\hat{\mathbf{x}}_{i'}}^{\mathbf{r}_{ii'}} \mathbf{J}_{\hat{\mathbf{x}}_i}^{\hat{\mathbf{x}}_{ii'}}, \quad (45)$$

$$\mathbf{J}_{\hat{\mathbf{x}}_{i'}}^{\mathbf{r}_{ii'}} = \mathbf{J}_{\hat{\mathbf{x}}_{ii'}}^{\mathbf{r}_{ii'}} \mathbf{J}_{\hat{\mathbf{x}}_{i'}}^{\hat{\mathbf{x}}_{ii'}}, \quad (46)$$

where $\mathbf{J}_{\hat{\mathbf{x}}_i}^{\hat{\mathbf{x}}_{ii'}} = -\mathbf{I}_3$, $\mathbf{J}_{\hat{\mathbf{x}}_{ii'}}^{\hat{\mathbf{x}}_{ii'}} = \mathbf{I}_3$.

Specifically, if we consider $h_{ii'}(\cdot)$ as a distance measurement function, the Jacobians can be calculated as

$$\mathbf{J}_{\hat{\mathbf{x}}_{ii'}}^{\mathbf{r}_{ii'}} = \frac{\hat{\mathbf{x}}_{ii'}}{\|\hat{\mathbf{x}}_{ii'}\|}. \quad (47)$$

B. Point-Line Measurement Jacobians

The measurement residual Jacobian with respect to the point i is

$$\mathbf{J}_{\hat{\mathbf{x}}_i}^{\mathbf{r}_{ij}} = \mathbf{J}_{\hat{\mathbf{p}}_{ij}}^{\mathbf{r}_{ij}} \mathbf{J}_{\hat{\mathbf{x}}_i}^{\hat{\mathbf{p}}_{ij}}, \quad (48)$$

where $\mathbf{J}_{\hat{\mathbf{x}}_i}^{\hat{\mathbf{p}}_{ij}} = \begin{bmatrix} \hat{\mathbf{n}}_j^\top \\ \hat{\mathbf{n}}_j^\top \times \hat{\mathbf{v}}_j^\top \end{bmatrix}$.

The measurement residual Jacobian with respect to the line estimation error is

$$\mathbf{J}_{\bar{\mathbf{p}}_j}^{\mathbf{r}_{ij}} = \mathbf{J}_{\bar{\mathbf{p}}_{ij}}^{\mathbf{r}_{ij}} \mathbf{J}_{\bar{\mathbf{l}}_j}^{\bar{\mathbf{p}}_{ij}}, \quad (49)$$

where

$$\mathbf{J}_{\bar{\mathbf{l}}_j}^{\bar{\mathbf{p}}_{ij}} = \begin{bmatrix} {}^G \hat{\mathbf{p}}_i [\hat{\mathbf{R}}_j \mathbf{e}_1]_{\times} & {}^G \hat{\mathbf{p}}_i \hat{\mathbf{R}}_j \mathbf{e}_1 \\ {}^G \hat{\mathbf{p}}_i [\hat{\mathbf{R}}_j \mathbf{e}_3]_{\times} & 1 \end{bmatrix},$$

and $\mathbf{J}_{\bar{\mathbf{p}}_j}^{\bar{\mathbf{l}}_j}$ is calculated in (40). When considering the measurement as point-line distance, $\mathbf{J}_{\bar{\mathbf{p}}_{ij}}^{\mathbf{r}_{ij}} = \frac{\hat{\mathbf{p}}_{ij}}{\|\hat{\mathbf{p}}_{ij}\|}$.

C. Point-Plane Measurement Jacobians

The measurement residual Jacobian with respect to the point estimate error is

$$\mathbf{J}_{\mathbf{x}_i}^{\mathbf{r}_{ij}} = \mathbf{G} \hat{\mathbf{n}}_k^T. \quad (50)$$

The measurement residual Jacobian with respect to the plane estimate error is

$$\mathbf{J}_{\hat{\mathbf{x}}_k}^{\mathbf{r}_{ij}} = \mathbf{J}_{\hat{\mathbf{p}}_k}^{\mathbf{r}_{ij}} \mathbf{J}_{\hat{\mathbf{x}}_k}^{\hat{\mathbf{p}}_{ij}}, \quad (51)$$

where

$$\mathbf{J}_{\hat{\mathbf{p}}_k}^{\mathbf{r}_{ij}} = [\mathbf{G} \hat{\mathbf{p}}_i^T \quad 1]^T,$$

and $\mathbf{J}_{\hat{\mathbf{x}}_k}^{\hat{\mathbf{p}}_{ij}}$ is provided in (42).

D. Line-Line Measurement Jacobians

The Jacobians of the measurement error $\alpha_{jj'}$ and $d_{jj'}$ w.r.t. the estimation error are

$$\mathbf{J}_{\hat{\mathbf{x}}_j}^{\alpha_{jj'}} = \mathbf{J}_{\hat{\mathbf{i}}_j}^{\alpha_{jj'}} \mathbf{J}_{\hat{\mathbf{x}}_j}^{\hat{\mathbf{i}}_j}, \quad (52)$$

where

$$\mathbf{J}_{\hat{\mathbf{i}}_j}^{\alpha_{jj'}} = \hat{\mathbf{v}}_j^T [(\hat{\mathbf{R}}_j \mathbf{e}_2)_{\times} \quad \mathbf{0}_{3 \times 1}].$$

The measurement residual Jacobian w.r.t. j' can be calculated similarly. Specifically, when two lines are parallel, namely $\hat{\mathbf{v}}_j = \pm \hat{\mathbf{v}}_{j'}$, the distance measurement Jacobian can be calculated as

$$\mathbf{J}_{\hat{\mathbf{x}}_j}^{\mathbf{r}_{jj'}^d} = \mathbf{J}_{\hat{\mathbf{i}}_j}^{\mathbf{r}_{jj'}^d} \mathbf{J}_{\hat{\mathbf{x}}_j}^{\hat{\mathbf{i}}_j}, \quad (53)$$

where

$$\mathbf{J}_{\hat{\mathbf{i}}_j}^{\mathbf{r}_{jj'}^d} = \hat{\mathbf{v}}_j' \times [d_j (\hat{\mathbf{R}}_j \mathbf{e}_1)_{\times} \quad \hat{\mathbf{R}}_j \mathbf{e}_1]. \quad (54)$$

E. Line-Plane Measurement Jacobians

The directional correlation measurement Jacobian is as follows

$$\mathbf{J}_{\hat{\mathbf{x}}_j}^{\mathbf{r}_{jk}^\alpha} = \mathbf{J}_{\hat{\mathbf{i}}_j}^{\mathbf{r}_{jk}^\alpha} \mathbf{J}_{\hat{\mathbf{x}}_j}^{\hat{\mathbf{i}}_j}, \quad (55)$$

where

$$\mathbf{J}_{\hat{\mathbf{i}}_j}^{\mathbf{r}_{jk}^\alpha} = [(\hat{\mathbf{R}}_j \mathbf{e}_3)_{\times} \quad \mathbf{0}_{3 \times 1}], \quad (56)$$

and

$$\mathbf{J}_{\hat{\mathbf{x}}_k}^{\mathbf{r}_{jk}^\alpha} = \frac{\hat{\mathbf{v}}_j^T (\mathbf{I}_3 - \mathbf{G} \hat{\mathbf{n}}_k \hat{\mathbf{n}}_k^T)}{\mathbf{G} \hat{d}_k}. \quad (57)$$

When the line j is parallel to the plane, namely $\hat{\mathbf{v}}_j^T \mathbf{n}_k = 0$, the distance residual Jacobians

$$\mathbf{J}_{\hat{\mathbf{x}}_j}^{\mathbf{r}_{jk}^d} = \mathbf{J}_{\hat{\mathbf{i}}_j}^{\mathbf{r}_{jk}^d} \mathbf{J}_{\hat{\mathbf{x}}_j}^{\hat{\mathbf{i}}_j}, \quad (58)$$

where

$$\mathbf{J}_{\hat{\mathbf{i}}_j}^{\mathbf{r}_{jk}^d} = \hat{\mathbf{n}}_k^T [(\hat{\mathbf{R}}_j \mathbf{e}_2)_{\times} \quad \hat{\mathbf{R}}_j \mathbf{e}_2], \quad (59)$$

and

$$\mathbf{J}_{\hat{\mathbf{x}}_k}^{\mathbf{r}_{jk}^d} = \frac{(\hat{\mathbf{n}}_j \times \hat{\mathbf{v}}_j)^T (\mathbf{I}_3 - \mathbf{G} \hat{\mathbf{n}}_k \hat{\mathbf{n}}_k^T) \mathbf{G} \hat{d}_j}{\mathbf{G} \hat{d}_k} + \mathbf{G} \hat{\mathbf{n}}_k^T. \quad (60)$$

F. Plane-Plane Measurement Jacobians

The Jacobian of the angle measurement residual is

$$\mathbf{J}_{\hat{\mathbf{x}}_k}^{\alpha_{kk'}} = \frac{(\hat{\mathbf{n}}_{k'})^T (\mathbf{I}_3 - \mathbf{G} \hat{\mathbf{n}}_k \hat{\mathbf{n}}_k^T)}{\mathbf{G} \hat{d}_k}. \quad (61)$$

The distance measurement residual is calculated as

$$\mathbf{J}_{\hat{\mathbf{x}}_k}^{\mathbf{r}_{kk'}^d} = \frac{\mathbf{G} \hat{\mathbf{p}}_k - \mathbf{G} \hat{\mathbf{p}}_{k'}}{\|\mathbf{G} \hat{\mathbf{p}}_k - \mathbf{G} \hat{\mathbf{p}}_{k'}\|} \quad (62)$$

The Jacobian w.r.t. the plane k' can be calculated similarly.

REFERENCES

- [1] G. Cai, J. Dias, and L. Seneviratne, "A survey of small-scale unmanned aerial vehicles: Recent advances and future development trends," *Unmanned Systems*, vol. 2, no. 02, pp. 175–199, 2014.
- [2] T.-M. Nguyen, S. Yuan, M. Cao, Y. Lyu, T. H. Nguyen, and L. Xie, "Viral-fusion: A visual-inertial-ranging-lidar sensor fusion approach," *arXiv preprint arXiv:2010.12274*, 2020.
- [3] H. Durrant-Whyte and T. Bailey, "Simultaneous localization and mapping: part i," *IEEE robotics & automation magazine*, vol. 13, no. 2, pp. 99–110, 2006.
- [4] H. Strasdat, J. Montiel, and A. J. Davison, "Scale drift-aware large scale monocular slam," *Robotics: Science and Systems VI*, vol. 2, no. 3, p. 7, 2010.
- [5] T. Sattler, B. Leibe, and L. Kobbelt, "Fast image-based localization using direct 2d-to-3d matching," in *2011 International Conference on Computer Vision*. IEEE, 2011, pp. 667–674.
- [6] P. Mühlfellner, M. Bürki, M. Bosse, W. Derendarz, R. Philippsen, and P. Furgale, "Summary maps for lifelong visual localization," *Journal of Field Robotics*, vol. 33, no. 5, pp. 561–590, 2016.
- [7] L. Platinsky, M. Szabados, F. Hlasek, R. Hemsley, L. Del Pero, A. Pancik, B. Baum, H. Grimmer, and P. Ondruska, "Collaborative augmented reality on smartphones via life-long city-scale maps," *ISMAR*, 2020.
- [8] S. Middelberg, T. Sattler, O. Untzelmann, and L. Kobbelt, "Scalable 6-dof localization on mobile devices," in *European conference on computer vision*. Springer, 2014, pp. 268–283.
- [9] T. Sattler, W. Maddern, C. Toft, A. Torii, L. Hammarstrand, E. Stenborg, D. Safari, M. Okutomi, M. Pollefeys, J. Sivic *et al.*, "Benchmarking 6dof outdoor visual localization in changing conditions," in *Proceedings of the IEEE Conference on Computer Vision and Pattern Recognition*, 2018, pp. 8601–8610.
- [10] N. Piasco, D. Sidibé, C. Demonceaux, and V. Gouet-Brunet, "A survey on visual-based localization: On the benefit of heterogeneous data," *Pattern Recognition*, vol. 74, pp. 90–109, 2018.
- [11] F. Dellaert, "Factor graphs and gtsam: A hands-on introduction," Georgia Institute of Technology, Tech. Rep., 2012.
- [12] L. Koppel and S. L. Waslander, "Manifold geometry with fast automatic derivatives and coordinate frame semantics checking in C++," *CoRR*, vol. abs/1805.01810, 2018. [Online]. Available: <http://arxiv.org/abs/1805.01810>
- [13] S. Weiss, D. Scaramuzza, and R. Siegwart, "Monocular-slam-based navigation for autonomous micro helicopters in gps-denied environments," *Journal of Field Robotics*, vol. 28, no. 6, pp. 854–874, 2011.
- [14] R. Mur-Artal, J. M. M. Montiel, and J. D. Tardós, "Orb-slam: A versatile and accurate monocular slam system," *IEEE Transactions on Robotics*, vol. 31, no. 5, pp. 1147–1163, 2015.
- [15] T. Qin, P. Li, and S. Shen, "Vins-mono: A robust and versatile monocular visual-inertial state estimator," *IEEE Transactions on Robotics*, vol. 34, no. 4, pp. 1004–1020, 2018.
- [16] T. Lemaire, C. Berger, I.-K. Jung, and S. Lacroix, "Vision-based slam: Stereo and monocular approaches," *International Journal of Computer Vision*, vol. 74, no. 3, pp. 343–364, 2007.
- [17] J. Zhang and S. Singh, "Loam: Lidar odometry and mapping in real-time," in *Robotics: Science and Systems*, vol. 2, no. 9, 2014.
- [18] J. Sturm, N. Engelhard, F. Endres, W. Burgard, and D. Cremers, "A benchmark for the evaluation of rgb-d slam systems," in *2012 IEEE/RSJ International Conference on Intelligent Robots and Systems*. IEEE, 2012, pp. 573–580.
- [19] R. P. Padhy, F. Xia, S. K. Choudhury, P. K. Sa, and S. Bakshi, "Monocular vision aided autonomous uav navigation in indoor corridor environments," *IEEE Transactions on Sustainable Computing*, vol. 4, no. 1, pp. 96–108, 2019.

- [20] Y. Lu and D. Song, "Robust rgb-d odometry using point and line features," in *The IEEE International Conference on Computer Vision (ICCV)*, December 2015.
- [21] A. Hasan, A. Qadir, I. Nordeng, and J. Neubert, "Construction inspection through spatial database," *arXiv preprint arXiv:1611.03566*, 2016.
- [22] T.-M. Nguyen, M. Cao, S. Yuan, Y. Lyu, T. H. Nguyen, and L. Xie, "Liro: Tightly coupled lidar-inertia-ranging odometry," *arXiv preprint arXiv:2010.13072*, 2020.
- [23] A. Chavez, D. L'Heureux, N. Prabhakar, M. Clark, W.-L. Law, and R. J. Prazenica, *Homography-Based State Estimation for Autonomous UAV Landing*. American Institute of Aeronautics and Astronautics, 2017. [Online]. Available: <https://arc.aiaa.org/doi/abs/10.2514/6.2017-0673>
- [24] A. Pumarola, A. Vakhitov, A. Agudo, A. Sanfeliu, and F. Moreno-Noguer, "PI-slam: Real-time monocular visual slam with points and lines," in *2017 IEEE international conference on robotics and automation (ICRA)*. IEEE, 2017, pp. 4503–4508.
- [25] Y. He, J. Zhao, Y. Guo, W. He, and K. Yuan, "PI-vio: Tightly-coupled monocular visual-inertial odometry using point and line features," *Sensors*, vol. 18, no. 4, p. 1159, 2018.
- [26] W. V. D. Hodge, W. Hodge, and D. Pedoe, *Methods of Algebraic Geometry: Volume 1*. Cambridge University Press, 1994, vol. 2.
- [27] Y. Yang, P. Geneva, P. Eckenhoff, and G. Huang, "Visual-inertial odometry with point and line features," in *2019 IEEE/RSJ International Conference on Intelligent Robots and Systems (IROS)*, 2019, pp. 2447–2454.
- [28] Y. Yang and G. Huang, "Aided inertial navigation: Unified feature representations and observability analysis," in *2019 International Conference on Robotics and Automation (ICRA)*. IEEE, 2019, pp. 3528–3534.
- [29] D. G. Kottas and S. I. Roumeliotis, "Efficient and consistent vision-aided inertial navigation using line observations," in *2013 IEEE International Conference on Robotics and Automation*. IEEE, 2013, pp. 1540–1547.
- [30] F. Zheng, G. Tsai, Z. Zhang, S. Liu, C.-C. Chu, and H. Hu, "Trifo-vio: Robust and efficient stereo visual inertial odometry using points and lines," in *2018 IEEE/RSJ International Conference on Intelligent Robots and Systems (IROS)*. IEEE, 2018, pp. 3686–3693.
- [31] R. Gomez-Ojeda, F.-A. Moreno, D. Zuñiga-Noël, D. Scaramuzza, and J. Gonzalez-Jimenez, "PI-slam: a stereo slam system through the combination of points and line segments," *IEEE Transactions on Robotics*, vol. 35, no. 3, pp. 734–746, 2019.
- [32] P. Geneva, K. Eckenhoff, Y. Yang, and G. Huang, "Lips: Lidar-inertial 3d plane slam," in *2018 IEEE/RSJ International Conference on Intelligent Robots and Systems (IROS)*. IEEE, 2018, pp. 123–130.
- [33] Y. Yang, P. Geneva, X. Zuo, K. Eckenhoff, Y. Liu, and G. Huang, "Tightly-coupled aided inertial navigation with point and plane features," in *2019 International Conference on Robotics and Automation (ICRA)*. IEEE, 2019, pp. 6094–6100.
- [42] P. J. Huber, "Robust estimation of a location parameter," in *Breakthroughs in statistics*. Springer, 1992, pp. 492–518.
- [34] J. Zhang, G. Zeng, and H. Zha, "Structure-aware slam with planes and lines in man-made environment," *Pattern Recognition Letters*, vol. 127, pp. 181–190, 2019.
- [35] Y. Yang and G. Huang, "Observability analysis of aided ins with heterogeneous features of points, lines, and planes," *IEEE Transactions on Robotics*, vol. 35, no. 6, pp. 1399–1418, 2019.
- [36] X. Li, Y. He, J. Lin, and X. Liu, "Leveraging planar regularities for point line visual-inertial odometry," *arXiv preprint arXiv:2004.11969*, 2020.
- [37] I. Aloise, B. D. Corte, F. Nardi, and G. Grisetti, "Systematic handling of heterogeneous geometric primitives in graph-slam optimization," *IEEE Robotics and Automation Letters*, vol. 4, no. 3, pp. 2738–2745, 2019.
- [38] F. Nardi, B. D. Corte, and G. Grisetti, "Unified representation and registration of heterogeneous sets of geometric primitives," *IEEE Robotics and Automation Letters*, vol. 4, no. 2, pp. 625–632, 2019.
- [39] I. Jovančević, I. Viana, J.-J. Ortu, T. Sentenac, and S. Larnier, "Matching cad model and image features for robot navigation and inspection of an aircraft," in *Proceedings of the 5th International Conference on Pattern Recognition Applications and Methods*, ser. ICPRAM 2016. Setubal, PRT: SCITEPRESS - Science and Technology Publications, Lda, 2016, p. 359–366. [Online]. Available: <https://doi.org/10.5220/0005756303590366>
- [40] M. Kaess, H. Johannsson, R. Roberts, V. Ila, J. J. Leonard, and F. Dellaert, "isam2: Incremental smoothing and mapping using the bayes tree," *The International Journal of Robotics Research*, vol. 31, no. 2, pp. 216–235, 2012.
- [41] C. Forster, L. Carlone, F. Dellaert, and D. Scaramuzza, "On-manifold preintegration for real-time visual-inertial odometry," *IEEE Transactions on Robotics*, vol. 33, no. 1, pp. 1–21, 2017.
- [43] M. Burri, J. Nikolic, P. Gohl, T. Schneider, J. Rehder, S. Omari, M. W. Achtelik, and R. Siegwart, "The euroc micro aerial vehicle datasets," *The International Journal of Robotics Research*, vol. 35, no. 10, pp. 1157–1163, 2016.
- [44] L. Carlone and S. Karaman, "Attention and anticipation in fast visual-inertial navigation," *IEEE Transactions on Robotics*, vol. 35, no. 1, pp. 1–20, 2019.
- [45] M. Shamaiah, S. Banerjee, and H. Vikalo, "Greedy sensor selection: Leveraging submodularity," in *49th IEEE conference on decision and control (CDC)*. IEEE, 2010, pp. 2572–2577.
- [46] R. A. Horn and C. R. Johnson, *Matrix analysis*. Cambridge university press, 2012.
- [47] B. Mirzasoleiman, A. Badanidiyuru, A. Karbasi, J. Vondrák, and A. Krause, "Lazier than lazy greedy," *arXiv preprint arXiv:1409.7938*, 2014.
- [48] Z. Zhang and D. Scaramuzza, "A tutorial on quantitative trajectory evaluation for visual(-inertial) odometry," in *IEEE/RSJ Int. Conf. Intell. Robot. Syst. (IROS)*, 2018.